ACS Partner Journal
PRECISION CHEMISTRY



pubs.acs.org/PrecisionChem
Article

# Unraveling the Effect of Stacking Configurations on Charge Transfer in $WS_2$ and Organic Semiconductor Heterojunctions

Shuchen Zhang,[¶] Dewei Sun,[¶] Jiaonan Sun, Ke Ma, Zitang Wei, Jee Yung Park, Aidan H. Coffey, Chenhui Zhu, Letian Dou,* and Libai Huang*

Cite This: *Precis. Chem.* 2023, 1, 443−451
Read Online

ACCESS | Metrics & More | Article Recommendations | Supporting Information

**ABSTRACT:** Photoinduced interfacial charge transfer plays a critical role in energy conversion involving van der Waals (vdW) heterostructures constructed of inorganic nanostructures and organic materials. However, the effect of molecular stacking configurations on charge transfer dynamics is less understood. In this study, we demonstrated the tunability of interfacial charge separation in a type-II heterojunction between monolayer (ML) $WS_2$ and an organic semiconducting molecule [2-(3″′,4′-dimethyl-[2,2′:5′,2″:5″,2″′-quaterthiophen]-5-yl)ethan-1-ammonium halide (4Tm)] by rational design of relative stacking configurations. The assembly between ML-$WS_2$ and the 4Tm molecule forms a face-to-face stacking when 4Tm molecules are in a self-aggregation state. In contrast, a face-to-edge stacking is observed when 4Tm molecule is incorporated into a 2D organic−inorganic hybrid perovskite lattice. The face-to-face stacking was proved to be more favorable for hole transfer from $WS_2$ to 4Tm and led to interlayer excitons (IEs) emission. Transient absorption measurements show that the hole transfer occurs on a time scale of 150 fs. On the other hand, the face-to-edge stacking resulted in much slower hole transfer without formation of IEs. This inefficient hole transfer occurs on a similar time scale as A exciton recombination in $WS_2$, leading to the formation of negative trions. These investigations offer important fundamental insights into the charge transfer processes at organic−inorganic interfaces.

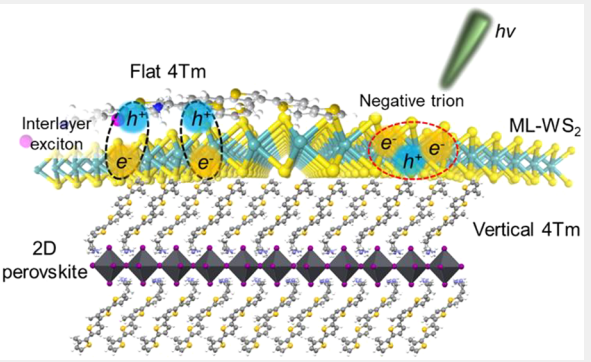


**KEYWORDS:** *Charge transfer, two-dimensional materials, organic semiconductors, heterojunction, stacking configuration, interlayer exciton*

## INTRODUCTION

Charge-transfer (CT) at heterointerfaces plays an essential role as intermediates with the increasing utilization of heterostructure materials in the energy conversion field.[1−4] It usually occurs in hybrid type-II heterojunctions through the separation of electrons and holes in adjacent layers with a gap of less than 1 nm.[5,6] Recently, robust models describing CT and excited state dynamics have been established in monolayer (ML) two-dimensional (2D) transition metal dichalcogenides (TMDCs).[7−11] Owing to the unique properties of TMDCs, such as atomic flatness, direct bandgap, strong light−matter interactions, and high charge transport mobility, their heterointerfaces with organic semiconducting molecules have been extensively explored to study the CT process.[12−14] In addition, organic−TMDC heterointerfaces are promising for cost-effective and efficient optoelectronic devices due to the high absorption efficiency of molecular semiconductors.

In contrast to conventional 2D heterostructures where CT is strongly coupled with the lattice degrees of freedom,[15,16] CT at organic−TMDC heterointerfaces is strongly dependent on the orientation and arrangement of the molecules at the interfaces.[17,18] For example, the organic semiconducting molecules with a conjugated plane can adopt two possible stacking configurations with TMDCs to form vertical heterostructures in principle.[19,20] One is that the conjugated plane of organic molecules lies parallel to the TMDC plane (face-on orientation), providing a large contact area and an in-plane transition dipole moment. The other stacking configuration involves the conjugated plane of organic molecules being oriented perpendicular to the TMDCs plane (edge-on orientation), exhibiting a small contact area and an out-of-plane transition dipole moment. However, there is currently a lack of a generally applicable method to control molecular orientation on TMDCs.[21,22]

The 2D organic−inorganic hybrid perovskites, known for their intriguing optoelectronic properties, could also serve as an effective framework for confining the orientation of organic

Received: April 30, 2023
Revised: June 6, 2023
Accepted: June 8, 2023
Published: June 26, 2023

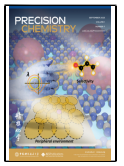





https://doi.org/10.1021/prechem.3c00057
*Precis. Chem.* 2023, 1, 443−451

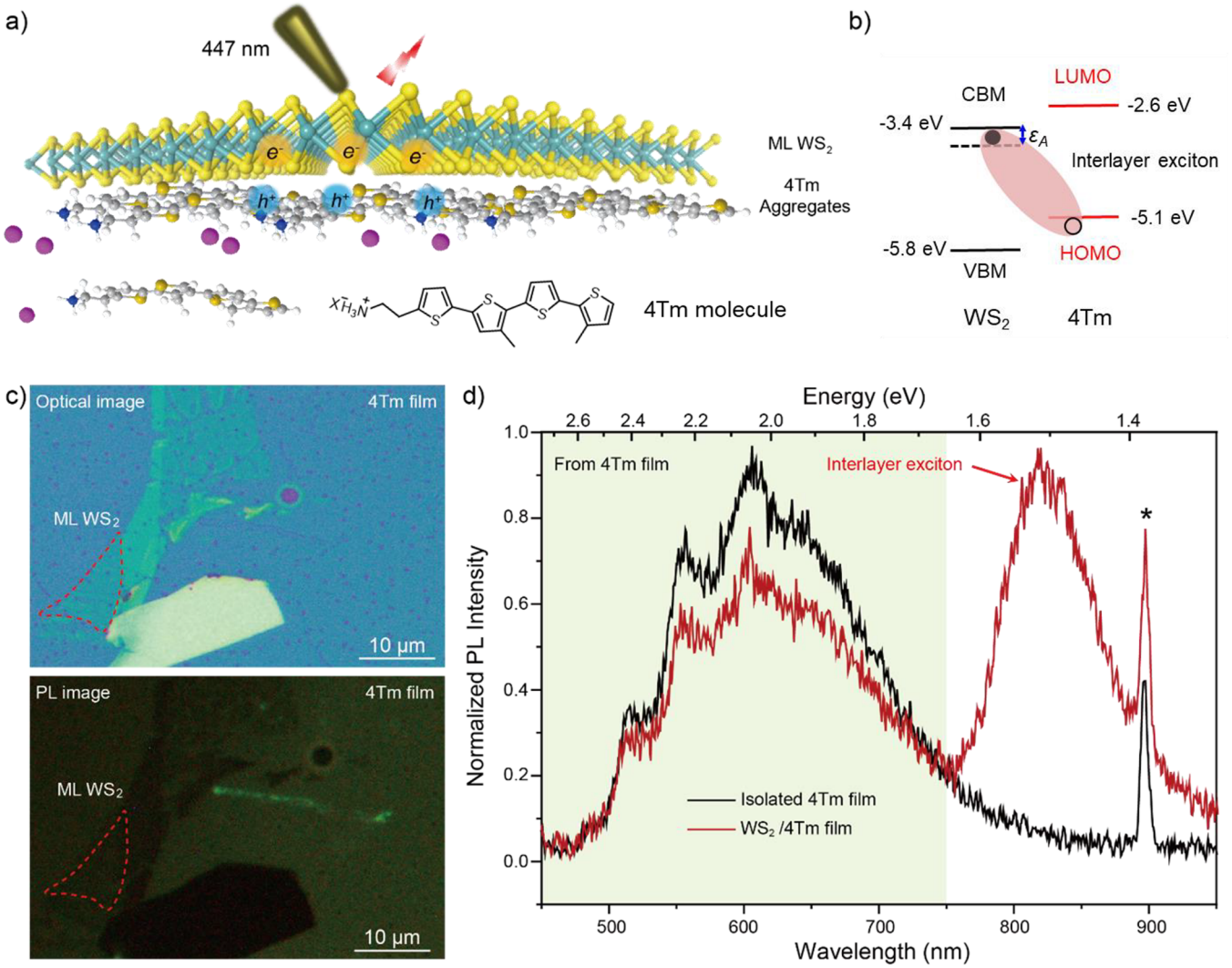


**Figure 1.** Face-to-face stacking of monolayer (ML) $WS_2$/4Tm film heterojunctions. (a) Scheme showing the face-to-face vertical stacking of ML-$WS_2$/4Tm film heterostructures and a laser with the wavelength of 447 nm (2.77 eV) used for optical measurements. (b) Band alignment between ML-$WS_2$ and 4Tm molecules, indicating a type-II junction and the possibility of forming interlayer excitons. Dash line indicates the exciton level, and $\varepsilon_A$ represents the binding energy. (c) Optical image and corresponding photoluminescence (PL) image of ML-$WS_2$/4Tm film heterojunction, indicating a severe PL quench for ML-$WS_2$. (d) Steady-state PL spectra of 4Tm thin film and ML-$WS_2$/4Tm film heterostructure at the temperature of 120 K. The new emission band at 1.51 eV indicates the formation of interlayer charge transfer (CT) excitons. *The asterisk mark represents the signal from the laser.

molecules with the assistance of atomically thin inorganic slabs.[23−26] For example, 2D Ruddlesden−Popper (RP) phase perovskites with a chemical formula of $L_2A_{n-1}B_nX_{3n+1}$, where L is a bulky ligand with either an alkyl or aromatic moiety, A is an organic cation, B is a metal cation, and X is a halide, can constrain the orientation of the L molecule in the out-of-plane direction.[27−29] Additionally, the bulky hydrophobic organic cations (or L ligands) can be designed to transition from insulating with large bandgaps to semiconducting with small bandgaps. Particularly, the 2D organic−inorganic hybrid perovskites with a designed organic semiconducting cation are considered "organic semiconductor-incorporated perovskites", or simply "OSiPs".[30,31] It provides an opportunity to create a different type of stacking configuration for organic semiconducting molecules and TMDCs, and to investigate the effects of stacking configurations on the CT process. Herein, we successfully designed two orientations of organic semiconducting molecules to realize different stacking configurations of their heterojunctions with ML-$WS_2$, and we clarified the effect of relative stacking configurations on the interfacial CT process. To acquire an additional orientation beyond the one in the self-aggregates, a quaterthiophene ammonium halide salt, 2-(3″′,4′-dimethyl-[2,2′:5′,2′:5″,2″′-quaterthiophen]-5-yl)ethan-1-ammonium halide (4Tm), standing nearly upright when incorporated into 2D perovskites,[32,33] was used as an organic semiconducting molecule and formed the type-II band alignment with ML-$WS_2$. Two kinds of stacking configurations, face-to-face and face-to-edge, were achieved through transferring ML-$WS_2$ onto 4Tm molecules that were either lying flat in self-aggregated film or standing nearly upright in 2D perovskites ($4Tm_2PbBr_4$), respectively. Using time-resolved and steady-state optical spectroscopy, a stacking configuration-dependent interfacial CT process was investigated. It was found that the face-to-face stacking was more favorable for CT, and the separated charges in $WS_2$ and 4Tm layer were bound at the vdW interface, leading the observation


https://doi.org/10.1021/prechem.3c00057
Precis. Chem. 2023, 1, 443−451

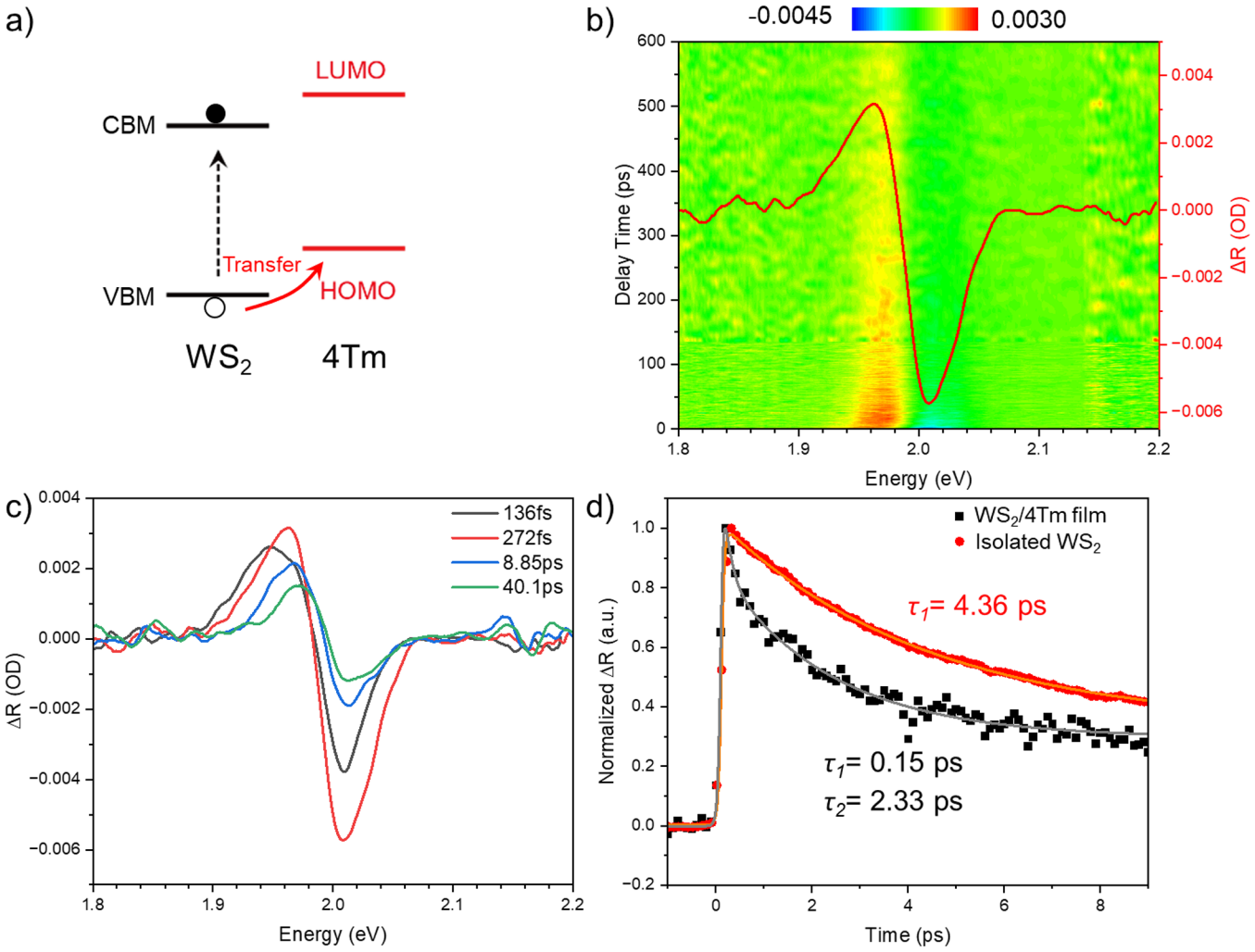


**Figure 2.** Hole transfer from ML-$WS_2$ to 4Tm molecule in a face-to-face stacking. (a) Band alignment showing the hole transfer process in the ML-$WS_2$/4Tm film heterostructure under excitation with a pump energy of 2.25 eV. (b) Transient absorption contour and a specific transient absorption spectrum at a pump−probe delay time of 272 fs after excitation at 550 nm (2.25 eV) for the ML-$WS_2$/4Tm heterojunction. (c) Transient absorption spectra of the ML-$WS_2$/4Tm heterojunction at three different time delays to investigate the hole transfer from $WS_2$ to 4Tm molecule. The pump excitation beam was tuned to 550 nm (2.25 eV). (d) Transient absorption dynamics of bare ML-$WS_2$ and ML-$WS_2$/4Tm pumped at 2.25 eV and probed at 2.0 eV. The dynamics of isolated $WS_2$ and ML-$WS_2$/4Tm film were fitted using exponential and biexponential decay functions, accordingly. Both of these functions were convoluted with the experimental response function.

of interlayer excitons (IEs). Transient absorption measurements show that the dissociation of $WS_2$ excitons occurred by hole transfer to 4Tm molecules on a time scale of 150 fs. In contrast, the face-to-edge stacking of $WS_2$ and 4Tm molecules in the 2D perovskite led to a much slower CT process that occurred in an inefficient way. This inefficiency also made it difficult to form IEs at the interface but did lead to the formation of negative trions within the $WS_2$ plane.

## RESULTS AND DISCUSSION

Thus far, numerous semiconducting organic molecules with various energy levels, such as 7-(thiophen-2-yl)-benzothiadiazol-4-yl)-[2,2′-bithiophen]-5-yl)ethylammonium (BTm),[34] 2-([2,2′-bithiophen]-5-yl)ethylammonium (2T),[33] and 4Tm,[32] have been designed to form 2D RP phase perovskites with type-I or type-II band alignments. However, to accurately capture the CT signal that is typically weak, it is important to minimize the background emission from the inorganic slabs of the 2D perovskite. In addition, as a candidate, the organic semiconducting molecule should also form a type-II heterojunction with TMDCs. Considering the aforementioned factors, the 4Tm molecule, known for its ability to form type-II 2D perovskites with no photoluminescence (PL) emission,[32] was selected to investigate the CT processes involved in different stacking configurations with ML-$WS_2$. Simultaneously, the lead-bromide (Pb−Br) perovskite matrix was chosen because of its wide band gap so that optical excitation inside the perovskite layer can be avoided in this study. In other words, the perovskite lattice was used only to control the orientation of the organic molecules.

First, a 4Tm film was prepared by spin-coating on a silicon substrate. This film exhibits an optical bandgap of ∼2.5 eV with a weak PL emission (Figure S1). The orientation of the 4Tm molecules was examined by X-ray diffraction (XRD), grazing incidence wide-angle X-ray scattering (GIWAXS) (Figure S2), and atomic force microscopy (AFM) (Figure S3). It was found that 4Tm molecules with a film thickness of ∼30 nm tend to lie flat on the substrate, which is similar to the behavior observed found in other organic molecules previously reported.[35] This prompts a face-to-face stacking configuration


https://doi.org/10.1021/prechem.3c00057
Precis. Chem. 2023, 1, 443−451

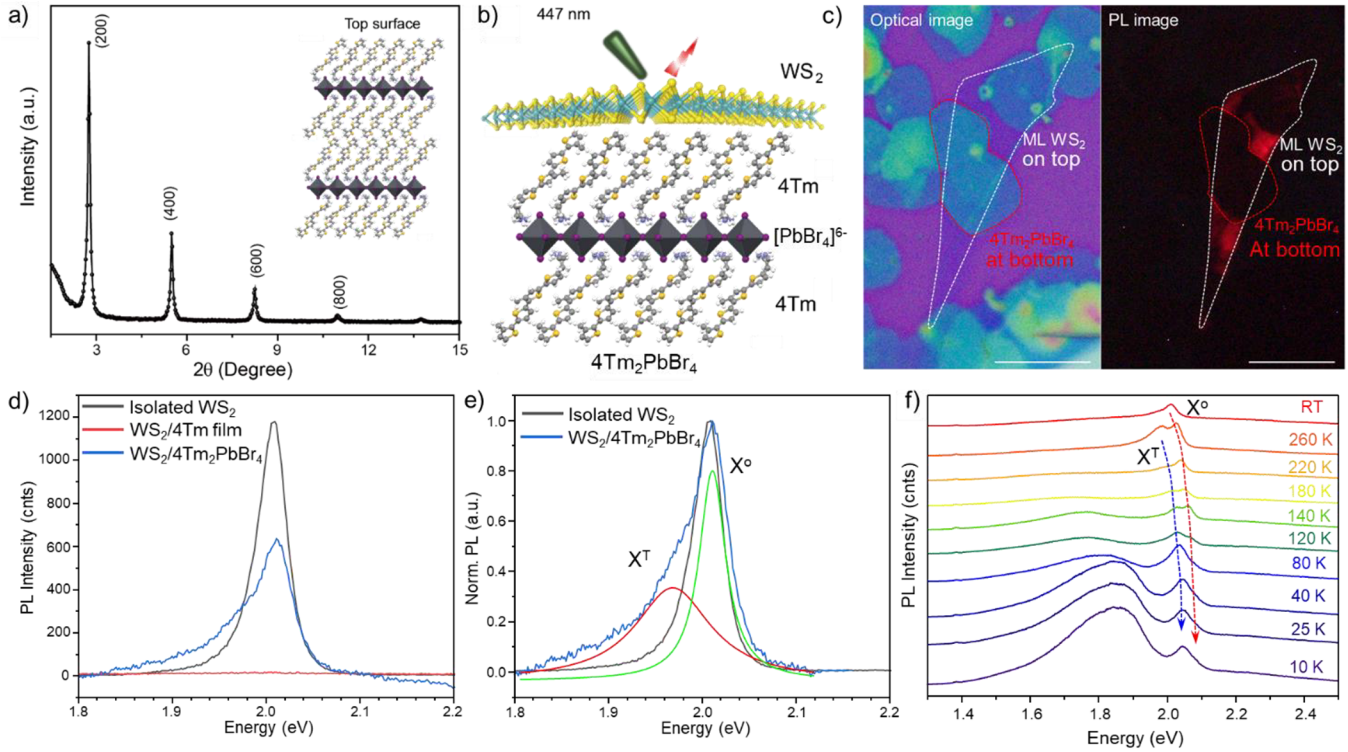


**Figure 3.** Face-to-edge vertical stacking of ML-$WS_2$/4Tm molecule heterojunction through incorporating 4Tm into 2D halide perovskite. (a) X-ray diffraction profile of the 2D perovskite using 4Tm as bulky ligands, simplified as $4Tm_2PbBr_4$. (b) Scheme showing the vertical stacking of the ML-$WS_2$ and $4Tm_2PbBr_4$ heterojunction and a laser with the wavelength of 447 nm used for optical measurements. (c) Optical image (left) and PL image (right) of a specific heterojunction fabricated by ML-$WS_2$ (top) and $4Tm_2PbBr_4$ (bottom). PL image indicates a slight PL quench for ML-$WS_2$. The scale bars are both 10 $\mu$m. (d) Steady-state PL spectra comparison among isolated $WS_2$, the ML-$WS_2$/4Tm junction, and the ML-$WS_2$/$4Tm_2PbBr_4$ junction at room temperature to quantify the difference led by stacking configurations. (e) Normalized PL spectra with peak fitting to indicate the formation of trions at the $WS_2$/$4Tm_2PbBr_4$ heterojunction. $X^0$ and $X^T$ represent A excitons and trions, respectively. (f) Temperature-dependent PL spectra of ML-$WS_2$/$4Tm_2PbBr_4$ heterojunction at temperatures from 10 to 295 K with the excitation energy of 2.77 eV (447 nm).

between 4Tm and ML-$WS_2$, as indicated in Figure 1a. Based on the respective energy levels of $WS_2$ and 4Tm molecule, a type-II band alignment is constructed, as illustrated in Figure 1b. The lowest unoccupied molecular orbital level (LUMO) (−2.6 eV)[32,33] of 4Tm molecules lies higher than the conduction band minimum (CBM) of ML-$WS_2$, whereas the valence band maximum (VBM) (−5.8 eV)[36] of $WS_2$ is located lower than the highest occupied molecular orbital (HOMO) level (−5.1 eV) of 4Tm molecules.[32,33] This type-II band alignment allows for electron transfer from 4Tm to $WS_2$ and hole collection by 4Tm upon optical excitation. Additionally, the analysis of the potential CT process implies the presence of CT IEs with an estimated energy of ∼1.7 eV. To confirm the existence of CT IEs, a flake of exfoliated ML-$WS_2$ was physically transferred onto the 4Tm film heterojunction, as shown in Figure 1c. The intense PL quenching at the junction area observed in the PL image can be attributed to the CT process due to the type-II band alignment.

Moreover, the steady-state PL spectra were taken to investigate the CT process with photoexcitation at 2.8 eV, which excites both the ML-$WS_2$ and the 4Tm molecules. The isolated 4Tm film exhibits a broad and weak emission peak (1.8−2.4 eV) due to the intramolecular interaction (Figure S4). In contrast to the isolated ML-$WS_2$ with a distinct PL emission on the substrate (Figure S5), the emission of the A exciton belonging to $WS_2$ at the heterojunction completely vanished, implying its efficient CT process with the 4Tm molecule. Further, temperature-dependent PL was conducted, revealing an additional low-energy emission peak at 1.51 eV from the heterojunction at temperatures lower than 140 K. This broad peak exhibits a gradually increased intensity as the temperature decreases (Figure 1d). We attribute this emission to the CT IEs, formed by the bound electrons and holes from the CBM of $WS_2$ and HOMO of 4Tm molecules, respectively. No emission from CT IEs was observed in the room-temperature PL spectrum (Figure S6). At room temperature, the IEs could relax through significant vibrations of the 4Tm molecules due to the thermal energy leading to fast nonradiative decay. As the temperature decreases, the molecular vibrations are gradually inhibited, which promotes the direct radiative recombination of the IEs and results in the observed emission. In addition, the binding energy of the IEs is estimated to be ∼0.2 eV based on the energy level diagram (Figure 1b) and comparable to that of IEs in heterostructures composed solely of TMDCs.[37] Moreover, the excitation-power-density dependence of the steady-state PL for IEs was analyzed at 10 K, implying a linear relationship between emission intensities and excitation power densities with a slope of 0.84 ($I \sim L^k$) (Figure S7). The slight deviation from the slope of 1 can be attributed to the exciton−exciton annihilation at high power density.[38]

Furthermore, transient absorption (TA) spectroscopy was employed to study the charge transfer dynamics in the ML-$WS_2$/4Tm film heterojunction with a face-to-face stacking configuration. The charge transfer process occurred only at the interface within a thickness of 2 nm. Specifically, the ML-$WS_2$/


https://doi.org/10.1021/prechem.3c00057
Precis. Chem. 2023, 1, 443−451

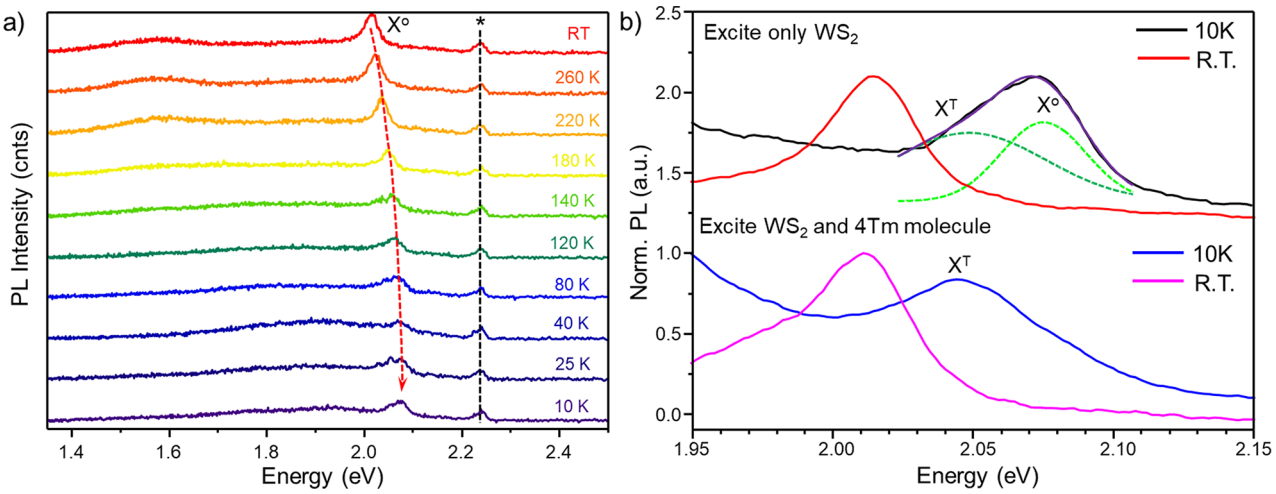


**Figure 4.** Temperature-dependent PL emission spectra of ML-$WS_2$/4$Tm_2PbBr_4$ heterojunction under selective excitation with a lower energy. (a) Specific temperature-dependent PL spectra of the ML-$WS_2$/4$Tm_2PbBr_4$ heterojunction excited at 550 nm (2.25 eV), which can only excite $WS_2$. *The asterisk mark represents the signal from laser with a wavelength of 550 nm. (b) Room temperature and low temperature PL spectra comparison under different optical excitation conditions for the ML-$WS_2$/4$Tm_2PbBr_4$ heterojunction. Top: collected PL results under the excitation of only $WS_2$ in the heterojunction. Bottom: collected PL results under the excitation of $WS_2$ and the 4Tm molecule in the heterojunction. The dashed lines are the fitting for the emission peak acquired under the excitation energy of 2.25 eV (550 nm) at 10 K. The fitting shows the coexistence of the A exciton and trion.

4Tm film heterojunction was excited with a pump energy of 2.25 eV that is below the absorption edge of 4Tm (Figure S1) to selectively investigate hole transfer from $WS_2$ to 4Tm molecule (Figure 2a). Figure 2b illustrates the TA contour, and with further extraction, Figure 2c shows a set of derivative-like signals in the ML-$WS_2$/4Tm heterojunction at the region of 2.0 eV, resembling the TA spectra of bare ML-$WS_2$ shown in Figures S8a and S9. These signals comprise an excited state absorption (ESA) at ∼1.97 eV and a ground state bleach (GSB) at ∼2.0 eV. The GSB at 2.0 eV corresponds to the A exciton, in agreement with the steady-state absorption of ML-$WS_2$.[36] The ESA at 1.98 eV features a major long-lived component and a short-lived tail at ∼1.9 eV, associated with trion and biexciton formation, respectively. The dynamics of the heterojunction and bare $WS_2$ probed at 2.0 eV were compared in Figure 2d. On the time scale of a few picoseconds, the dynamics of the heterostructure decays much faster than that of bare $WS_2$, attributable to the hole transfer from the VBM of $WS_2$ to the HOMO of 4Tm, as illustrated in Figure 2a. At the same time, a long-lived tail is discernible in the decay of the heterojunction within an extended time window (Figure S8b), revealing the nature of the charge separation between ML-$WS_2$ and 4Tm layers. Further, the decays of the isolated ML-$WS_2$ and heterojunction were fitted with exponential and biexponential decay functions, yielding an additional fast component with a time constant of ∼0.15 ps in the heterostructure. The fast hole transfer explains the efficient quenching of A exciton emission and is significantly faster than that in tetracene-TMDCs heterojunction.[36,39]

Next, we investigate the face-to-edge stacking configuration by incorporating 4Tm molecules into 2D halide perovskites. The 2D perovskite (4$Tm_2PbBr_4$) thin sheets were synthesized by using a solvent-evaporation method, and their structure was confirmed by XRD and GIWAXS, as shown in Figures 3a and S10. Both of these results are in agreement with the existing literature.[32] It is noteworthy that, in the 2D perovskite, 4Tm molecules are vertically oriented with a certain incline angle to the inorganic slabs of the 2D perovskites and maintain the similar energy level structure as implied by the absorption spectra (Figure S11). A face-to-edge contact between $WS_2$ and 4Tm molecules was formed when $WS_2$ was transferred onto the 2D perovskite surface, as depicted in Figure 3b. According to the energy band alignment as illustrated in Figure S12, the HOMO of the 4Tm molecule occupies the highest energy level compared with the VBM of ML-$WS_2$ and Pb−Br slab, facilitating the hole transfer from inorganic layers to organic 4Tm layers. However, two possible pathways for electron transfer exist, as both the CBM of $WS_2$ and Pb−Br slab can accept electrons from the 4Tm molecule. Obviously, the presence of a Pb−Br slab in the perovskite introduces extra energy bands, which also potentially participate in the CT as illustrated in Figure S12 and increase the complexity of the heterostructure system. To eliminate this effect on investigation of stacking configuration, the detailed optical measurements were conducted to elucidate the specific process using a small excitation energy (∼2.77 eV), which cannot excite the Pb−Br layer with a larger band gap (∼3.02 eV), in the heterojunction of ML-$WS_2$ and 4$Tm_2PbBr_4$ perovskite.

Figure 3c (left) displays an optical image of the specific heterojunction formed by ML-$WS_2$ and 4$Tm_2PbBr_4$, both of which possess flat surfaces, as implied by the AFM image (Figure S13). The corresponding PL image is presented in Figure 3c (right), displaying an evident PL quenching at both the junction and the 2D perovskite itself due to the type-II band alignments. The observed PL quenching indicates that CT can occur at the interfaces between the inorganic layers (ML-$WS_2$ and Pb−Br slabs) and the organic 4Tm layers. To quantify PL quenching, steady-state room-temperature PL spectra were collected in a specific heterostructure fabricated by ML-$WS_2$ and 4$Tm_2PbBr_4$. As shown in Figure 3d, the PL intensity of $WS_2$ at the heterojunction is quenched by only half, which is dramatically different from the complete PL quenching at the ML-$WS_2$/4Tm film interface with a very efficient CT. The differences in the degree of PL quenching between the two kinds of heterojunctions imply a less efficient CT process in a face-to-edge contact between $WS_2$ and organic


https://doi.org/10.1021/prechem.3c00057
Precis. Chem. 2023, 1, 443−451

molecules. In addition, with peak fitting for the quenched PL spectrum of $WS_2$ (Figure 3e), it is concluded that a noticeable trion peak at ∼1.97 eV coexists with the A exciton at the heterojunction. In contrast, the PL intensity of the trion peak is almost negligible on isolated $WS_2$.

To further investigate the effect of face-to-edge configuration on the CT process, the temperature-dependent PL was carried out on the ML-$WS_2$/4Tm$_2$PbBr$_4$ perovskite heterojunction and summarized in Figures 3f and S14−S17. With an excitation energy of 2.77 eV, both the ML-$WS_2$ and the 4Tm molecules (in the perovskite matrix) are excited, while the lead-bromide perovskite matrix remains unexcited. From room temperature to 180 K, the spectra show a blue shift in the exciton emission of ML-$WS_2$ due to an enlarged bandgap led by the lattice contraction.[40] Between 260 and 120 K, the emission peak is split into two distinct peaks with an energy difference of ∼60 meV. For the two peaks, the higher-energy peak is assigned as A exciton, while the lower-energy peak is attributed to the trion emission.[41−43] However, no IEs emission was observed at low energy area (<1.6 eV) for the junction. Interestingly, a distinctive difference at a high energy area (∼2.0 eV) in PL emission between the individual ML-$WS_2$ (Figure S14) and the heterojunction is discerned. Particularly, at a temperature of 10 K, the PL spectrum of the individual ML-$WS_2$ exhibits multiple peaks, attributed to A exciton and trion emission due to doping, lattice contraction, or intrinsic defects (Figure S14). On the other hand, the formation of the unique trion in the ML-$WS_2$/4Tm$_2$PbBr$_4$ perovskite heterojunction can be understood by the type-II band alignment (i.e., electron transfer from the LUMO of 4Tm to the CBM of ML-$WS_2$). Therefore, the observed trion is likely negatively charged. Overall, these observations show significant differences from the results of face-to-face $WS_2$-4Tm stacking discussed above, suggesting that the stacking configuration of ML-$WS_2$ and the 4Tm molecule can significantly impact the CT process.

To determine these pathways responsible for generating extra electrons to bind the A excitons to form negative trions, we performed PL measurements using an excitation energy of 2.25 eV, which can only excite ML-$WS_2$ yet neither the 4Tm molecule nor the inorganic slab (Pb−Br) of the 2D perovskite. As shown in Figure 2a, according to the band alignment, only one possible CT process could occur, which is the hole transfer from the VBM of $WS_2$ to the HOMO of 4Tm. The temperature-dependent PL measurement was performed (Figure 4a), and it was found that only one broad emission peak from $WS_2$ in the heterojunction is retained with a continuous blue shift until the temperature decreases to 9 K. In Figure 4b, the enhanced trion emission is shown when both $WS_2$ and 4Tm are excited at 9 K, compared to when only $WS_2$ is excited. Thus, it can be inferred that 4Tm plays a more dominant role in injecting electrons into the conduction band of $WS_2$, leading to the formation of negative trions upon the excitation of 4Tm molecules. In contrast, trion formation through capturing the excess electron left on $WS_2$ after the hole transfer to the 4Tm molecule is less efficient in the face-to-edge stacking configuration. This is in good agreement with the less efficient PL quenching shown in Figure 3d. The underlying reason is that the transfer of holes from $WS_2$ to the 4Tm molecule is relatively slow, occurring on a similar time scale as A exciton recombination. As a result, A exciton emission is not completely quenched.

## CONCLUSIONS

In summary, we designed two stacking configurations for the vertical type-II heterojunction composed of ML-$WS_2$ and organic semiconducting molecule (4Tm), including face-to-face stacking based on free-distributed 4Tm molecules in a thin film and face-to-edge stacking realized by incorporating 4Tm into a 2D hybrid perovskite. The CT process was found to be strongly dependent on the relative stacking configurations at the organic−TMDC heterointerface. Charge separation on the order of 150 fs was observed for the face-to-face configuration and was significantly slowed down for face-to-edge configuration. Additionally, the heterojunctions between $WS_2$ and 2D perovskite provide a model system to investigate the CT involving two heterointerfaces with consideration of additional lead-halide slab, which has not yet been explored. These investigations provide new opportunities for the design of efficient charge separation processes[44] in energy conversion applications by rationally engineering the interfaces between organic and inorganic semiconductors using 2D perovskites as scaffolds.

## EXPERIMENTAL METHODS

### Preparation of 4Tm Film

4Tm molecule was synthesized using the previously reported method,[32] and the purity was evaluated by nuclear magnetic resonance (NMR). To acquire the thin film sample, such as 4Tm film, generally, 5 mg of 4Tm was dissolved in 100 μL of dimethylformamide (DMF) to prepare a 0.1 M ligand solution. Twenty μL of 4Tm ligand solution was dispensed on a clean Si substrate, followed by spin-coating at 2000 rpm for 30 s. Later, the thin film was annealed at 150 °C on a hot plate for 10 min. The ligand solution preparation and spin-coating process were conducted in glovebox.

### Preparation of 4Tm$_2$PbBr$_4$ Nanocrystals

The solvent evaporation method, similar to the one reported,[33] was adopted to obtain 2D halide perovskite nanocrystals. For example, to acquire 4Tm$_2$PbBr$_4$ nanocrystal, a stock solution with the concentration of 5 mM was prepared by dissolving 10 μmol of $PbBr_2$ and 20 μmol of 4TmBr in 2 mL of DMF/chlorobenzene cosolvent (1:1 volume ratio). The stock solution was then diluted 240 times using a cosolvent of chlorobenzene/acetonitrile/dichlorobenzene (3.9:1:0.01 volume ratio). Then a 5−10 μL amount of diluted solution was added onto the growth substrate $SiO_2$ (300 nm)/Si, which was placed at the bottom of a 4 mL glass vial. Then, the vial was placed onto a 90 °C hot plate for 15 min to acquire the 2D perovskites.

### Fabrication of the Vertical Heterojunctions

The ML-$WS_2$ is mechanically exfoliated onto the polydimethylsiloxane (PDMS) substrate and then dry-transferred using a point-to-point transfer method onto the top surface of 4Tm molecular film or 2D halide perovskite.

### Steady-State PL Measurements

The steady-state PL measurements were performed using a 40× [numerical aperture (NA), 0.60] objective in a home-built microscope setup. In the measurements, a laser light generated by a picosecond-pulsed diode (LDH-P-C-450B, PicoQuant) with a 2.8 eV excitation energy (full width at half-maximum, 50 ps) was focused by the objective. Temperature-dependent (ranging from 9 to 298 K) steady-state PL measurements were carried out in a helium cooled cryostation (MONTANA INSTRUMENT). The optical imaging, including bright and dark field images, was collected using a custom microscope (Olympus BX53).


https://doi.org/10.1021/prechem.3c00057
Precis. Chem. 2023, 1, 443−451

### Transient Absorption Spectroscopy

TA spectroscopy utilizes a custom-built femtosecond pump−probe setup, as described in detail in a previous publication.[45] The experimental setup consisted of an optical parametric amplifier (OPA) driven by 1030 nm fundamental light from an amplified Yb:KGW laser system with a 750 kHz repetition rate. The OPA generated a pump at 550 nm, while a portion of the fundamental light was directed onto a YAG crystal to generate a broadband probe light spanning from 480 to 800 nm. An optical chopper modulated the pump at a frequency of 195 Hz, and a motorized linear stage controlled the time delay between the pump and the probe, providing a maximum delay of approximately 1 ns. The pump and probe beams were overlapped and focused on the sample by using a 40x objective with a numerical aperture of 0.6. The reflected light was collected by the same objective and directed toward a spectrometer for analysis. To prevent exposure to air and moisture during measurements, the samples were housed in a vacuum chamber (ST-500, Janis).

### AFM Measurements

AFM images were recorded in tapping mode using an atomic force microscope (Bruker MultiMode 8).

### XRD Measurements

XRD was measured by using a powder X-ray diffractometer (Panalytical Empyrean) with a Cu K$\alpha$ source. The wavelength ($\lambda$) was 0.154 nm. The XRD measurements were performed on the as-grown 2D perovskites covering almost the entire surface of the $SiO_2$ (300 nm)/Si substrate.

### Grazing Incidence Wide-Angle X-ray Scattering Characterization

GIWAXS spectra were collected at beamline 7.3.3 at the Advanced Light Source at Lawrence Berkeley National Lab utilizing an incident angle of 0.1° and a wavelength of 1.24 Å (10 keV X-rays). The 2D spectra were taken with a Pilatus 2 M (Dectris) 2D detector, converted into the q space using a standard silver behenate sample, and reduced to 1D lines with the Igor Pro NIKA GIWAXS package software.[46] Raw data were further processed and visualized using Xi-Cam.[47]

## ■ ASSOCIATED CONTENT

### Supporting Information

The Supporting Information is available free of charge at https://pubs.acs.org/doi/10.1021/prechem.3c00057.

Additional data and figures including optical measurements on individual ML-$WS_2$, AFM images, absorption spectra, GIWAXS data, and more analysis on PL spectra (PDF)

## ■ AUTHOR INFORMATION


### Corresponding Authors

**Letian Dou** − *Davidson School of Chemical Engineering and Birck Nanotechnology Center, Purdue University, West Lafayette, Indiana 47907, United States;* orcid.org/0000-0001-6411-8591; Email: dou10@purdue.edu

**Libai Huang** − *Department of Chemistry, Purdue University, West Lafayette, Indiana 47907, United States;* orcid.org/0000-0001-9975-3624; Email: libai-huang@purdue.edu

### Authors

**Shuchen Zhang** − *Davidson School of Chemical Engineering, Purdue University, West Lafayette, Indiana 47907, United States*

**Dewei Sun** − *Department of Chemistry, Purdue University, West Lafayette, Indiana 47907, United States*

**Jiaonan Sun** − *Davidson School of Chemical Engineering, Purdue University, West Lafayette, Indiana 47907, United States;* orcid.org/0000-0002-4102-0564

**Ke Ma** − *Davidson School of Chemical Engineering, Purdue University, West Lafayette, Indiana 47907, United States*

**Zitang Wei** − *Davidson School of Chemical Engineering, Purdue University, West Lafayette, Indiana 47907, United States*

**Jee Yung Park** − *Davidson School of Chemical Engineering, Purdue University, West Lafayette, Indiana 47907, United States*

**Aidan H. Coffey** − *Advanced Light Source, Lawrence Berkeley National Laboratory, Berkeley, California 94720, United States*

**Chenhui Zhu** − *Advanced Light Source, Lawrence Berkeley National Laboratory, Berkeley, California 94720, United States*

Complete contact information is available at: https://pubs.acs.org/10.1021/prechem.3c00057


### Author Contributions

¶S.Z. and D.S. contributed equally.

### Notes

The authors declare no competing financial interest.

## ■ ACKNOWLEDGMENTS

This work is primarily supported by the US Department of Energy, Office of Basic Energy Sciences under award number DE-SC0022082. The views expressed herein do not necessarily represent the views of the U.S. Department of Energy or the United States Government. L.D. acknowledges support from National Science Foundation under award number 2143568-DMR.

## ■ REFERENCES


(1) Zhu, X.; Monahan, N. R.; Gong, Z.; Zhu, H.; Williams, K. W.; Nelson, C. A. Charge Transfer Excitons at van der Waals Interfaces. *J. Am. Chem. Soc.* **2015**, *137*, 8313−8320.

(2) Vandewal, K.; Albrecht, S.; Hoke, E. T.; Graham, K. R.; Widmer, J.; Douglas, J. D.; Schubert, M.; Mateker, W. R.; Bloking, J. T.; Burkhard, G. F.; Sellinger, A.; Fréchet, J. M. J.; Amassian, A.; Riede, M. K.; McGehee, M. D.; Neher, D.; Salleo, A. Efficient Charge Generation by Relaxed Charge-transfer States at Organic Interfaces. *Nat. Mater.* **2014**, *13*, 63−68.

(3) Jariwala, D.; Marks, T. J.; Hersam, M. C. Mixed-dimensional van der Waals Heterostructures. *Nat. Mater.* **2017**, *16*, 170−181.

(4) Liu, X.; Gu, J.; Ding, K.; Fan, D.; Hu, X.; Tseng, Y. W.; Lee, Y. H.; Menon, V.; Forrest, S. R. Photoresponse of an Organic Semiconductor/Two-Dimensional Transition Metal Dichalcogenide Heterojunction. *Nano Lett.* **2017**, *17*, 3176−3181.

(5) Jin, C.; Ma, E. Y.; Karni, O.; Regan, E. C.; Wang, F.; Heinz, T. F. Ultrafast Dynamics in van der Waals Heterostructures. *Nat. Nanotechnol.* **2018**, *13*, 994−1003.

(6) Ma, H.; Wang, Z.; Zhao, W.; Ren, H.; Zhu, H.; Chi, Y.; Guo, W. Enhancing the Photoinduced Interlayer Charge Transfer and Spatial Separation in Type-II Heterostructure of $WS_2$ and Asymmetric Janus-MoSSe with Intrinsic Self-Build Electric Field. *J. Phys. Chem. Lett.* **2022**, *13*, 8484−8494.

(7) Yuan, L.; Zheng, B.; Kunstmann, J.; Brumme, T.; Kuc, A. B.; Ma, C.; Deng, S.; Blach, D.; Pan, A.; Huang, L. Twist-angle-dependent Interlayer Exciton Diffusion in $WS_2$-$WSe_2$ Heterobilayers. *Nat. Mater.* **2020**, *19*, 617−623.

(8) Kozawa, D.; Carvalho, A.; Verzhbitskiy, I.; Giustiniano, F.; Miyauchi, Y.; Mouri, S.; Neto, A. H. C.; Matsuda, K.; Eda, G.

Evidence for Fast Interlayer Energy Transfer in $MoSe_2/WS_2$ Heterostructures. *Nano Lett.* **2016**, *16*, 4087−4093.
(9) Wang, K.; Huang, B.; Tian, M.; Ceballos, F.; Lin, M.; Mahjouri-Samani, M.; Boulesbaa, A.; Puretzky, A. A.; Rouleau, C. M.; Yoon, M.; Zhao, H.; Xiao, K.; Duscher, G.; Geohegan, D. B. Interlayer coupling in twisted $WSe_2/WS_2$ bilayer heterostructures revealed by optical spectroscopy. *ACS Nano* **2016**, *10*, 6612−6622.
(10) Deilmann, T.; Thygesen, K. S. Interlayer Trions in the $MoS_2/WS_2$ van der Waals Heterostructure. *Nano Lett.* **2018**, *18*, 1460−1465.
(11) Chen, H.; Wen, X.; Zhang, J.; Wu, T.; Gong, Y.; Zhang, X.; Yuan, J.; Yi, C.; Lou, J.; Ajayan, P. M.; Zhang, G.; Zheng, J. Ultrafast formation of interlayer hot excitons in atomically thin $MoS_2/WS_2$ heterostructures. *Nat. Commun.* **2016**, *7*, 12512.
(12) Liu, X.; Gu, J.; Ding, K.; Fan, D.; Hu, X.; Tseng, Y.; Lee, Y.; Menon, V.; Forrest, S. R. Photoresponse of an organic semiconductor/two-dimensional transition metal dichalcogenide heterojunction. *Nano Lett.* **2017**, *17*, 3176−3181.
(13) Huang, Y.; Zhuge, F.; Hou, J.; Lv, L.; Luo, P.; Zhou, N.; Gan, L.; Zhai, T. Van der Waals coupled organic molecules with monolayer $MoS_2$ for fast response photodetectors with gate-tunable responsivity. *ACS Nano* **2018**, *12*, 4062−4073.
(14) Zheng, Y. J.; Huang, Y. L.; Chen, Y.; Zhao, W.; Eda, G.; Spataru, C. D.; Zhang, W.; Chang, Y.; Li, L.; Chi, D.; Quek, S. Y.; Wee, A. T. S. Heterointerface screening effects between organic monolayers and monolayer transition metal dichalcogenides. *ACS Nano* **2016**, *10*, 2476−2484.
(15) He, M.; Rivera, P.; Van Tuan, D.; Wilson, N. P.; Yang, M.; Taniguchi, T.; Watanabe, K.; Yan, J.; Mandrus, D. G.; Yu, H.; Dery, H.; Yao, W.; Xu, X. Valley phonons and exciton complexes in a monolayer semiconductor. *Nat. Commun.* **2020**, *11*, 618.
(16) Chen, D.; Lian, Z.; Huang, X.; Su, Y.; Rashetnia, M.; Yan, L.; Blei, M.; Taniguchi, T.; Watanabe, K.; Tongay, S.; Wang, Z.; Zhang, C.; Cui, Y.; Fei, S. Tuning moiré excitons and correlated electronic states through layer degree of freedom. *Nat. Commun.* **2022**, *13*, 4810.
(17) Maiti, S.; Poonia, D.; Schiettecatte, P.; Hens, Z.; Geiregat, P.; Kinge, S.; Siebbeles, L. D. A. Generating triplets in organic semiconductor tetracene upon photoexcitation of transition metal dichalcogenide $ReS_2$. *J. Phys. Chem. Lett.* **2021**, *12*, 5256−5260.
(18) Padgaonkar, S.; Amsterdam, S. H.; Bergeron, H.; Su, K.; Marks, T. J.; Hersam, M. C.; Weiss, E. A. Molecular-orientation-dependent interfacial charge transfer in phthalocyanine/$MoS_2$ mixed-dimensional heterojunctions. *J. Phys. Chem. C* **2019**, *123*, 13337−13343.
(19) Chen, W.; Huang, H.; Chen, S.; Huang, Y. L.; Gao, X. Y.; Wee, A. T. S. Molecular orientation-dependent ionization potential of organic thin films. *Chem. Mater.* **2008**, *20*, 7017−7021.
(20) Chen, W.; Qi, D. C.; Huang, H.; Gao, X.; Wee, A. T. S. Organic−organic heterojunction interfaces: Effect of molecular orientation. *Adv. Funct. Mater.* **2011**, *21*, 410−424.
(21) Mativetsky, J. M.; Kastler, M.; Savage, R. C.; Gentilini, D.; Palma, M.; Pisula, W.; Müllen, K.; Samorì, P. Self-Assembly of a Donor-Acceptor Dyad Across Multiple Length Scales: Functional Architectures for Organic Electronics. *Adv. Funct. Mater.* **2009**, *19*, 2486−2494.
(22) Anariba, F.; Viswanathan, U.; Bocian, D. F.; McCreery, R. L. Determination of the structure and orientation of organic molecules tethered to flat graphitic carbon by ATR-FT-IR and Raman spectroscopy. *Anal. Chem.* **2006**, *78*, 3104−3112.
(23) Dou, L.; Wong, A. B.; Yu, Y.; Lai, M.; Kornienko, N.; Eaton, S. W.; Fu, A.; Bischak, C. G.; Ma, J.; Ding, T.; Ginsberg, N. S.; Wang, L.; Alivisatos, A. P.; Yang, P. Atomically thin two-dimensional organic-inorganic hybrid perovskites. *Science* **2015**, *349*, 1518−1521.
(24) Park, I. H.; Chu, L.; Leng, K.; Choy, Y. F.; Liu, W.; Abdelwahab, I.; Zhu, Z.; Ma, Z.; Chen, W.; Xu, Q. H.; Eda, G.; Loh, K. P. Highly Stable Two-Dimensional Tin (II) Iodide Hybrid Organic−Inorganic Perovskite Based on Stilbene Derivative. *Adv. Funct. Mater.* **2019**, *29*, 1904810.
(25) Li, C.; Loh, K. P.; Leng, K. Organic-inorganic Hybrid Perovskites and their Heterostructures. *Matter* **2022**, *5*, 4153−4169.
(26) Shi, E.; Gao, Y.; Finkenauer, B. P.; Akriti; Coffey, A. H.; Dou, L. Two-dimensional halide perovskite nanomaterials and heterostructure. *Chem. Soc. Rev.* **2018**, *47*, 6046−6072.
(27) Shao, Y.; Gao, W.; Yan, H.; Li, R.; Abdelwahab, I.; Chi, X.; Rogée, L.; Zhuang, L.; Fu, W.; Lau, S. P.; Yu, S. F.; Cai, Y.; Loh, K. P.; Leng, K. Unlocking surface octahedral tilt in two-dimensional Ruddlesden-Popper perovskites. *Nat. Commun.* **2022**, *13*, 138.
(28) Yu, Y.; Zhang, D.; Yang, P. Ruddlesden−Popper Phase in Two-dimensional Inorganic Halide Perovskites: a Plausible Model and the Supporting Observations. *Nano Lett.* **2017**, *17*, 5489−5494.
(29) Chen, Y.; Sun, Y.; Peng, J.; Tang, J.; Zheng, K.; Liang, Z. 2D Ruddlesden−Popper perovskites for optoelectronics. *Adv. Mater.* **2018**, *30*, 1703487.
(30) Gao, Y.; Dou, L. Organic Semiconductor-incorporated Two-dimensional Halide Perovskites. *Nat. Sci. Rev.* **2022**, *9*, nwab111.
(31) Zhao, W.; Hsu, S. N.; Boudouris, B. W.; Dou, L. Two-dimensional organic semiconductor-incorporated perovskite (OSiP) electronic. *ACS Appl. Electron. Mater.* **2021**, *3*, 5155−5164.
(32) Gao, Y.; Shi, E.; Deng, S.; Shiring, S. B.; Snaider, J. M.; Liang, C.; Yuan, B.; Song, R.; Janke, S. M.; Liebman-Peláez, A.; Yoo, P.; Zeller, M.; Boudouris, B. W.; Liao, P.; Zhu, C.; Blum, V.; Yu, Y.; Savoie, B. M.; Huang, L.; Dou, L. Molecular engineering of organic−inorganic hybrid perovskites quantum wells. *Nat. Chem.* **2019**, *11*, 1151−1157.
(33) Shi, E.; Yuan, B.; Shiring, S. B.; Gao, Y.; Akriti; Guo, Y.; Su, C.; Lai, M.; Yang, P.; Kong, J.; Savoie, B. M.; Yu, Y.; Dou, L. Two-dimensional halide perovskite lateral epitaxial heterostructures. *Nature* **2020**, *580*, 614−620.
(34) Wang, K.; Jin, L.; Gao, Y.; Liang, A.; Finkenauer, B. P.; Zhao, W.; Wei, Z.; Zhu, C.; Guo, T.; Huang, L.; Dou, L. Lead-free organic−perovskite hybrid quantum wells for highly stable light-emitting diodes. *ACS Nano* **2021**, *15*, 6316−6325.
(35) Gujral, A.; Gómez, J.; Jiang, J.; Huang, C.; O'Hara, K. A.; Toney, M. F.; Chabinyc, M. L.; Yu, L.; Ediger, M. D. Highly organized smectic-like packing in vapor-deposited glasses of a liquid crystal. *Chem. Mater.* **2017**, *29*, 849−858.
(36) Zhu, T.; Yuan, L.; Zhao, Y.; Zhou, M.; Wan, Y.; Mei, J.; Huang, L. Highly mobile charge-transfer excitons in two-dimensional $WS_2$/tetracene heterostructures. *Sci. Adv.* **2018**, *4*, eaao3104.
(37) Wilson, N. R.; Nguyen, P. V.; Seyler, K.; Rivera, P.; Marsden, A. J.; Laker, Z. P. L.; Constantinescu, G. C.; Kandyba, V.; Barinov, A.; Hine, N. D. M.; Xu, X.; Cobden, D. H. Determination of Band Offsets, Hybridization, and Exciton Binding in 2D Semiconductor Heterostructures. *Sci. Adv.* **2017**, *3*, e1601832.
(38) Yuan, L.; Huang, L. Exciton Dynamics and Annihilation in $WS_2$ 2D Semiconductors. *Nanoscale* **2015**, *7*, 7402−7408.
(39) Bettis Homan, S.; Sangwan, V. K.; Balla, I.; Bergeron, H.; Weiss, E. A.; Hersam, M. C. Ultrafast exciton dissociation and long-lived charge separation in a photovoltaic pentacene−$MoS_2$ van der Waals heterojunction. *Nano Lett.* **2017**, *17*, 164−169.
(40) Park, H.; Shin, G. H.; Lee, K. J.; Choi, S. Y. Probing temperature-dependent interlayer coupling in a $MoS_2$/h-BN heterostructure. *Nano Res.* **2020**, *13*, 576−582.
(41) Kesarwani, R.; Simbulan, K. B.; Huang, T. D.; Chiang, Y. F.; Yeh, N. C.; Lan, Y. W.; Lu, T. H. Control of trion-to-exciton conversion in monolayer $WS_2$ by orbital angular momentum of light. *Sci. Adv.* **2022**, *8*, eabm0100.
(42) Shi, J.; Li, Y.; Zhang, Z.; Feng, W.; Wang, Q.; Ren, S.; Zhang, J.; Du, W.; Wu, X.; Sui, X.; Mi, Y.; Wang, R.; Sun, Y.; Zhang, L.; Qiu, X.; Lu, J.; Shen, C.; Zhang, Y.; Zhang, Q.; Liu, X. Twisted-angle-dependent optical behaviors of intralayer excitons and trions in $WS_2$/$WSe_2$ heterostructure. *ACS Photonics* **2019**, *6*, 3082−3091.
(43) Shi, J.; Zhu, J.; Wu, X.; Zheng, B.; Chen, J.; Sui, X.; Zhang, S.; Shi, J.; Du, W.; Zhong, Y.; Wang, Q.; Zhang, Q.; Pan, A.; Liu, X. Enhanced trion emission and carrier dynamics in monolayer $WS_2$ coupled with plasmonic nanocavity. *Adv. Opt. Mater.* **2020**, *8*, 2001147.
(44) Leng, K.; Wang, L.; Shao, Y.; Abdelwahab, I.; Grinblat, G.; Verzhbitskiy, I.; Li, R.; Cai, Y.; Chi, X.; Fu, W.; Song, P.; Rusydi, A.;

Eda, G.; Maier, S. A.; Loh, K. P. Electron tunneling at the molecularly thin 2D perovskite and graphene van der Waals interface. *Nat. Commun.* **2020**, *11*, 5483.
(45) Guo, Z.; Wan, Y.; Yang, M.; Snaider, J.; Zhu, K.; Huang, L. Long-range hot-carrier transport in hybrid perovskites visualized by ultrafast microscopy. *Science* **2017**, *356*, 59−62.
(46) Ilavsky, J. Nika: software for two-dimensional data reduction. *J. Appl. Crystallogr.* **2012**, *45*, 324−328.
(47) Pandolfi, R. J.; Allan, D. B.; Arenholz, E.; Barroso-Luque, L.; Campbell, S. I.; Caswell, T. A.; Blair, A.; De Carlo, F.; Fackler, S.; Fournier, A. P.; Freychet, G.; Fukuto, M.; Gürsoy, D.; Jiang, Z.; Krishnan, H.; Kumar, D.; Kline, R. J.; Li, R.; Liman, C.; Marchesini, S.; Mehta, A.; N'Diaye, A. T.; Parkinson, D. Y.; Parks, H.; Pellouchoud, L. A.; Perciano, T.; Ren, F.; Sahoo, S.; Strzalka, J.; Sunday, D.; Tassone, C. J.; Ushizima, D.; Venkatakrishnan, S.; Yager, K. G.; Zwart, P.; Sethian, J. A.; Hexemer, A. Xi-cam: a versatile interface for data visualization and analysis. *J. Synchrotron Rad.* **2018**, *25*, 1261−1270.


https://doi.org/10.1021/prechem.3c00057
*Precis. Chem.* 2023, 1, 443−451